Some comments on mapping the combined effects of slurry concentration, impact velocity and electrochemical potential on the erosion- corrosion of WC/Co-Cr coatings

M.M. Stack and T. M Abd El-Badia

Department of Mechanical Engineering,

University of Strathclyde, James Weir Building,

75 Montrose St., Glasgow,

G1 1XJ, UK

Abstract

Materials exposed to aqueous slurry environments must not only resist the impact of solid particles and the flowing environment but also the degradation caused by electrochemical corrosion. In this study, the combined effects of slurry particle concentration and velocity on the erosion –corrosion of a WC/Co-Cr coating were assessed at a range of electrochemical potentials in a synthetic sea water solution containing sand particles and compared to the performance of a mild steel exposed to similar conditions. The erosion and corrosion contributions and their interactions were evaluated for the materials. The results indicated that the erosion-corrosion mechanism of the coating and the mild steel showed significant differences when particle velocity and concentration were increased at various potentials. For both materials, degradation

mechanisms were identified and superimposed on erosion-corrosion maps. Maps indicating levels of wastage, extent of synergy between the processes and the optimum material performance were also generated as part of this study. Scanning electron microscopy was used to confirm the degradation regimes and mechanisms of material removal during the erosion-corrosion process.

Key words: erosion-corrosion maps; WC/Co-Cr coatings, slurry solutions, synergy/additive effect maps; materials performance maps

1. Introduction

Thermally sprayed coatings are used to improve the wear characteristics of surfaces since they combine several attractive features i.e. resistance to abrasion, erosion, high temperature and corrosive atmospheres [1]. High velocity oxy-fuel (HVOF) coatings have been used widely in many engineering components for combating wear and corrosion. Components coated by the HVOF method include propellers, pump impellers and casings, valve bodies and pipe systems. Numerous researches have been directed towards the development of spraying conditions, and characterization of the specific abrasive and erosive wear resistances of the coatings [2].

Erosion–corrosion is a significant materials issue in many industries including oil and gas production, mining and material processing. In such cases, components such as pumps, valves, agitators, petrol explorer equipments and pipelines are in contact with aqueous slurries during operation [3, 4]. Removal of the surface films formed during

the corrosion process by particles such as silica sand can accelerate the degradation of the material. On the other hand, corrosion can have a deleterious effect on the mechanical properties of the material making it more susceptible to wear, particularly in the case of multi-phase materials such as composites [3].

Recent research on the erosion–corrosion of materials in aqueous conditions has attempted to provide various criteria for the predominance of erosion–corrosion mechanisms in aqueous conditions [5-8]. This has been carried out in order to deconvolute a very complex process involving a very large range of mechanical and chemical phenomena. The regimes range from erosion to corrosion dominated depending on the response of the material to the attack of the corrosive slurry. A methodology has been developed to define criteria for such regime transitions as a function of the ratio of the erosion to corrosion rate [5-8].

In studies of erosion-corrosion of composite based coatings to date, a significant issue has been that there has been very little attempt to identify the wastage mechanisms over a wide range of conditions. In addition, the extent of synergy between the erosion and corrosion process has not been characterized over this performance window, which limits the application of the research.

The aim of this paper is to address this issue by investigating the erosion-corrosion behaviour of a WC/Co-Cr thermally sprayed coating and mild steel, over a range of conditions. The effects of slurry particle concentration and the impact velocity on the erosion-corrosion behaviour were investigated at various applied potentials in synthetic

sea water containing silica sand. Finally, erosion–corrosion maps were developed showing the change in erosion–corrosion mechanisms, wastage rates and extent of synergy between the two processes. The results were also used to generate material performance maps based on the test conditions.

2. Experimental details

2.1 Materials

The erosion-corrosion tests were performed on mild steel (the coating substrate) and a WC/Co-Cr coating. Optical Microscopy and Electron Dispersive X-Ray Analysis (EDX) for the WC/Co-Cr coating, Figs. 1-2, were carried out to investigate the thickness and the percentages of the carbides and binder phases in the coatings, as shown in Table 1, respectively. The thickness of the coating varied in the range of 8-13 μm, Fig. 2. The dimension of specimens was 20 X 10 X 3 mm, however only a small area was exposed to impingement; the remaining area was covered by tape. The surface area of the samples exposed to the slurry jet was 0.1963 cm^2.

2.2 Test procedure

The slurry erosion resistance of all the samples was determined by mass loss measurements. The samples were weighed before and after the test to an accuracy of ±0.10 mg using a precision balance (a Mettler electronic balance). The test samples were set at a fixed impact angle of 90° to the impinging jet. Erosion-corrosion tests were conducted for 30 minutes. At the end of the test, the samples were removed and cleaned with distilled water and acetone to remove any slurry or debris. Each test was repeated 3 times. The experimental error was within ±15%. Specimens were examined prior to and after testing to investigate the microstructure and mechanisms of damage using a scanning electron microscope (SEM).

Table 1: Composition of the coating tested

Element	C	Cr	Co	W
Wt %	9.9	5.02	14.14	70.94

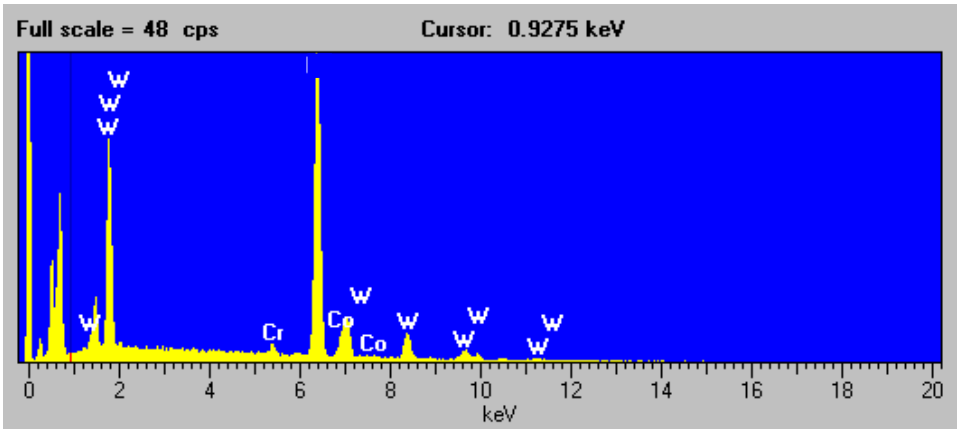

Fig.1: EDX analysis of the coating [6]

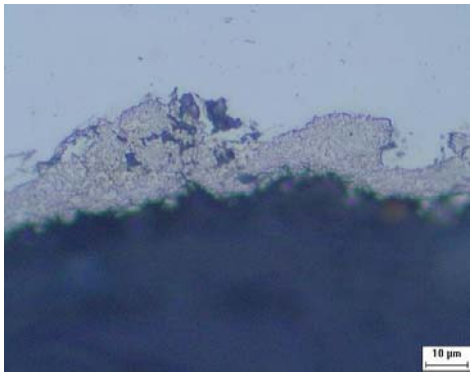

Fig. 2: Optical microscopy of cross section of the coating morphology [6]

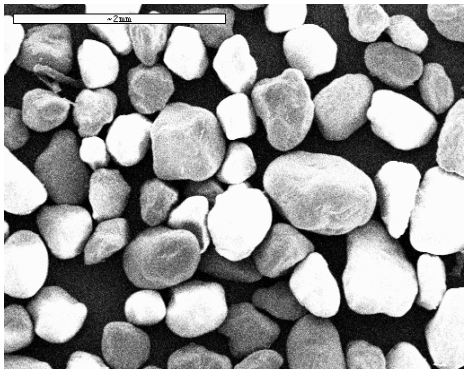

Fig. 3: Silica sand used in the erosion–corrosion tests

2.3 Erosion-corrosion tests

Erosion–corrosion experiments in this work were performed using an impinging jet apparatus (detailed elsewhere; [9]) which comprised a liquid–solid jet generated from a recirculating system as shown in Fig.4. The particle concentration of the slurry was varied at three values 4%, 6% and 8% (by mass %), and at two impact velocities namely 2 and 4 ms^{-1}. The slurry was composed of silica sand, with a size in the range 50 to 250 μm, Fig. 3, (20 wt. % particles to 80% solution) in synthetic sea water (prepared according to ASTM D 1141-98) as electrolyte. Polarisation curves were measured at the required slurry concentration and velocity from -700 to 700 mV at a sweep rate of 1 mV s^{-1} with a pre-treatment at -700 mV for 60 s prior to the initiation of the potential sweep to remove any residual air-formed oxide film.

In potentiostatic conditions, erosion–corrosion tests were performed at potentials of-600, 0, 250, 500 mV for a half hour by using a computer controlled ACM (GILLAC) potentiostat. The electrochemical interface attached to the rig was configured as shown in Fig. 5. It should be noted that due to solution resistance, there was a drop in the applied potential for the mild steel [10]. Hence, the potential values for the mild steel have been corrected to reflect this (the original potentials for the mild steel were similar to those for the coating). For the WC coating, the current densities recorded were significantly lower than the mild steel. In this case, the IR drop was considered not to be significant.

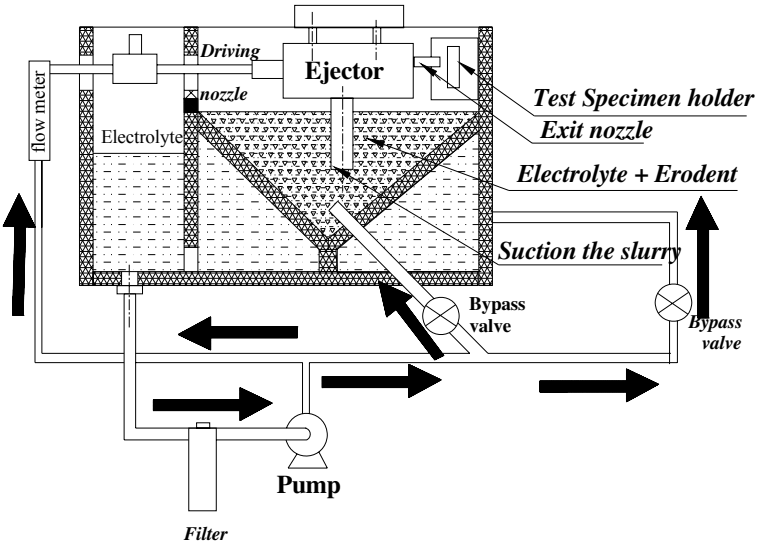

Fig. 4: Slurry impingement erosion test rig based on the design of Zu et al [9].

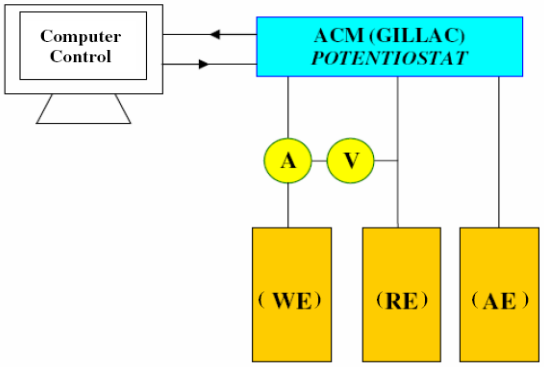

Fig. 5: The electrochemical configuration of the three electrode cell used in the erosion-corrosion tests

2.4 Calculation of corrosion contribution

The mass loss due to erosion-corrosion, as defined total wastage, was measured as described above. The corrosion contribution was calculated by Faraday's law:

$$M = I\ t\ a / (n\ F) \quad (1)$$

where M = mass loss, I = current in Amperes, t = time in seconds, F = Faraday's constant, n = electron valence of the metal and m= atomic mass of metal.

3. Results

3.1 Erosion corrosion wastage data

The erosion-corrosion wastage has been defined in previous work [5-8, 11], as follows:

$$K_{ec}=K_c+K_e \quad (2)$$

where, K_{ec} is the mass loss due to erosion-corrosion, K_e is the mass loss due to erosion and K_c is mass loss due to the corrosion. Figs. 6-7 show the mass loss rate due to erosion-corrosion and its contributions (K_e and K_c) for the coated and uncoated materials function of applied potentials at 3 slurry concentrations at an impact velocity of 2 ms^{-1}.

For both materials, there was a general increase in the wastage rates with applied potential, particularly at the high values. The effect of slurry concentration appeared to be more significant at high potential values. There was a similarity in the erosion-corrosion rate pattern for the two target materials; however the magnitude of mass loss for the mild steel was greater than that for the WC/Co-Cr coating. For this material, the corrosion contribution appeared to be dependent on applied potential, and particle concentration, with a general increase with applied potential only at the higher particle concentrations, Fig. 6c.

Figs. 8-9 represents the mass loss rate due to erosion-corrosion at 4 applied potentials and 3 slurry concentrations, at 4 ms^{-1}. Again, the uncoated material (mild steel) showed a higher high mass loss rate in these conditions compared with the coated material and the rate of increase reached a maximum at higher potentials.

The results for the coating indicated a generally similar trend to that observed at lower velocities, Fig. 6-7, in that there was an increase in erosion-corrosion rate with increasing applied potential. However, the change in erosion and corrosion rates with increasing potential was less clear, with no clear trend as a function of increasing potential.

(a) 4% slurry concentration

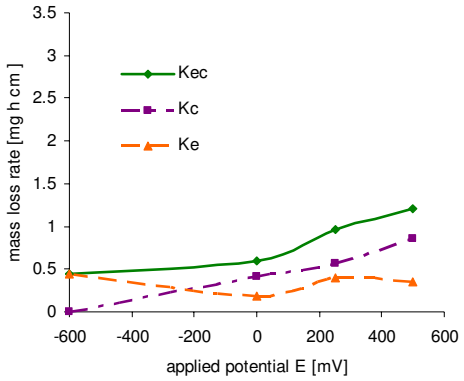

(b) 6% slurry concentration

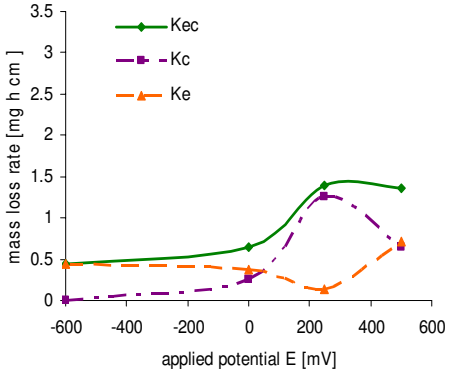

(c) 8% slurry concentration

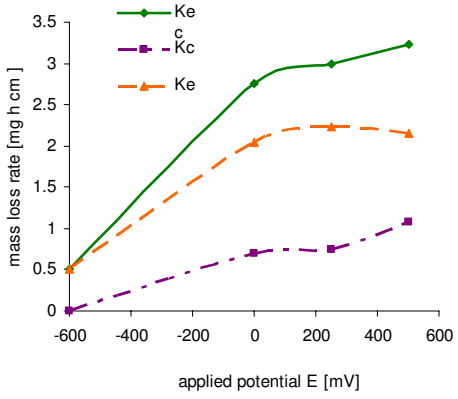

Fig. 6: Mass loss rates for the WC/Co-Cr coating as a function of applied potential at 2 ms^{-1} impact velocity

(a) 4% slurry concentration

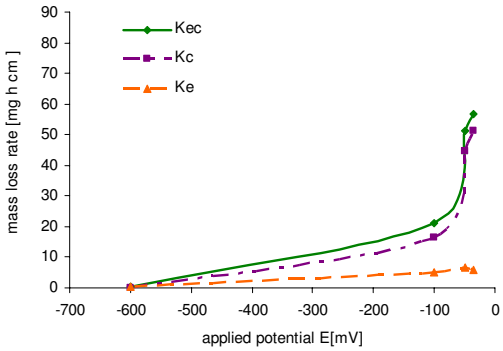

(b) 6% slurry concentration

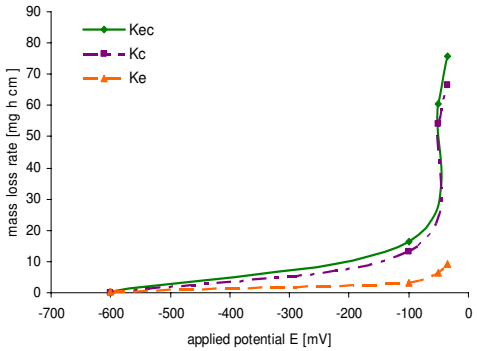

(c) 8% slurry concentration

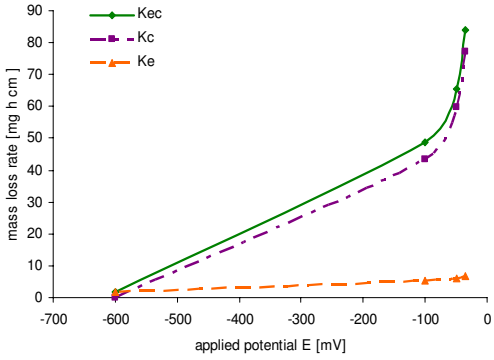

Fig. 7: Mass loss rates for mild steel as a function of applied potential at 2 ms^{-1} impact velocity

(a) 4% slurry concentration

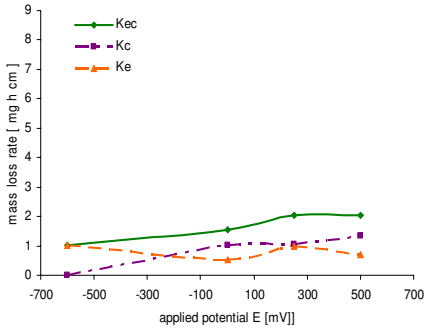

(b) 6% slurry concentration

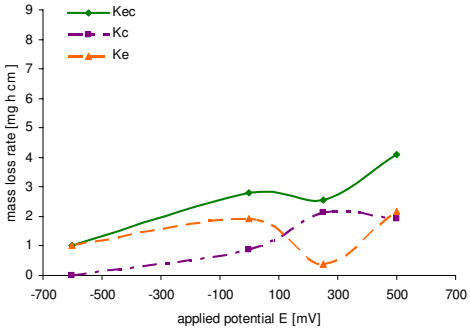

(c) 8% slurry concentration

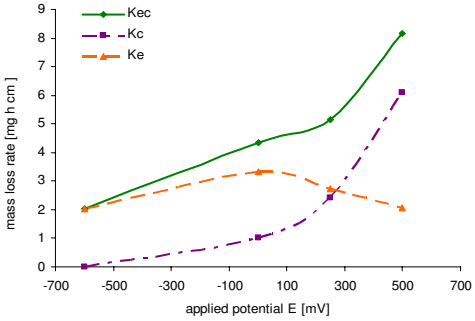

Fig. 8: Mass loss rates for the WC/Co-Cr coating as a function of applied potential at 4 ms^{-1} impact velocity

(a) 4% slurry concentration

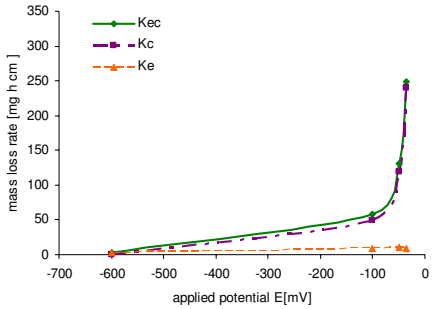

(b) 6% slurry concentration

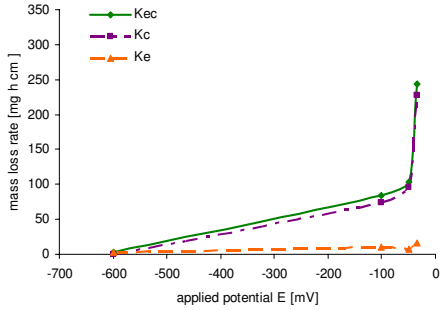

(c) 8% slurry concentration

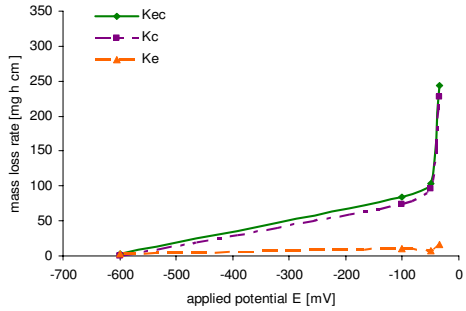

Fig. 9: Mass loss rates for mild steel as a function of applied potential at 4 ms^{-1} impact velocity

3.2 Electrochemical monitoring

Polarization tests were conducted in sea water conditions in various erosion conditions as follows:

1) v= 2 ms^{-1} at 4, 6 and 8% slurry particle concentrations.

2) v= 4 ms^{-1} at 4, 6 and 8% slurry particle concentrations.

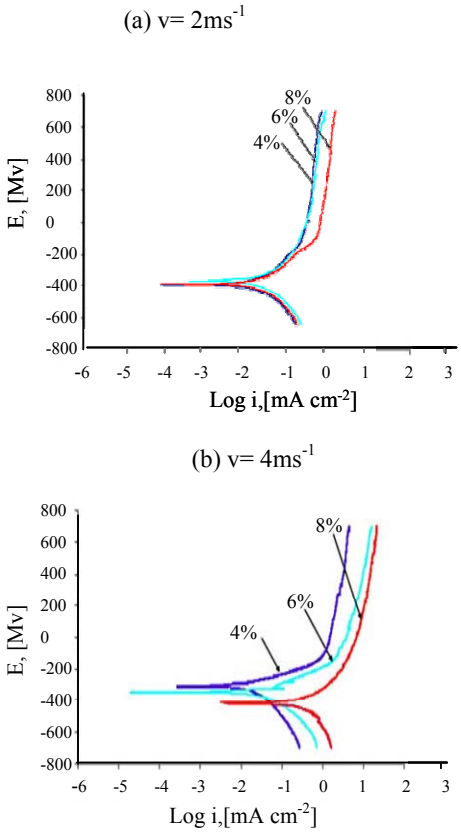

Fig. 10: Polarization curve for the WC/Co-Cr coating

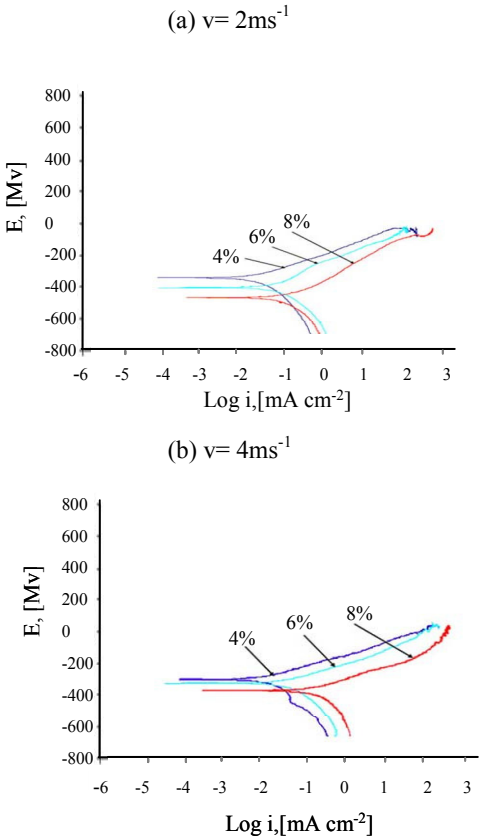

Fig. 11: Polarization curve for mild steel

The results, Figs. 10-11, indicated that at both velocities there was a tendency for the anodic current density to increase with increasing slurry concentration for the coated and uncoated steel. For both materials, the corrosion potential shifted to lower values

with increasing particle concentration. The values of the anodic current densities also appeared to increase with increasing velocity, Figs. 10-11. For the mild steel, these current density values were higher than for the coating, implying better corrosion resistance of the WC/Co-Cr coating compared with the mild steel.

4. Discussion

4.1 Mechanisms of corrosion and erosion–corrosion as a function of impact velocity and slurry concentration at different electrochemical conditions

It is clear that from the erosion-corrosion data and polarization behaviour, Figs. 6-11, that the trends for mild steel and the coating differ significantly. For the mild steel, the variation of current density and erosion-corrosion rate with velocity and concentration shows (Figs. 7, 9 and 11) a clear increase in the magnitude of wastage with increases in these parameters. That is possibly due to a combination of two phenomena; an increase in mechanical deformation leading to greater amount of surface area available for attack by the corrosive media, as shown on the scanning electron micrographs, Fig. 12, and the effects of increased transport of oxygen in the solution at higher velocities i.e. mass transport effects [12]. Both of these processes occurring simultaneously would significantly enhance the corrosion and erosion rate, in the event of the corrosion product not adhering to the surface. It is likely that ferrous ions are oxidized to ferric ions within the mass transfer diffusion layer further leading to the development of layers which may be readily removed during the erosion-corrosion process [13]. The removal

of loosely adherent surface films would thus result in the increase in the anodic current densities [19] as observed in Fig. 11.

The results for the coating Figs. 6, 8 and 10, differ significantly from those for mild steel, Figs. 7, 9 and 11 as the particle concentration is increased. The magnitude of mass loss is almost two orders less for the coating for the components K_e, K_c and K_{ec} values at both velocities. There is some evidence of a retardation or reduction in corrosion rate and corresponding erosion-corrosion rate at intermediate concentration values and at high potentials. The erosion-corrosion process of the composite will consist of competition between dissolution at the interface between the WC particles and the matrix, formation of a protective chromium oxide film over the Ni-Cr surface of the corrosion at the interface and removal of the particles and surface film. It is likely that there are changes in mechanisms of erosion-corrosion at the higher potentials and that, as we are dealing with a two phase system, more than one corrosion regime is interacting with the erosion process. It is also possible that sand particles are depositing on the surfaces and that salt deposits from the corrosion process are also modifying the weight change pattern. (For the purpose of mapping the regime transitions, we have no means of distinguishing the subtle changes in behaviour at such potentials and we assume that the dissolution of the interface between the carbides and the matrix material to be the predominant corrosion process as a first approximation). Metallographic analysis, Fig 12-13, shows a comparison between the plastic deformation and gouging type features observed on the mild steel, Fig. 12, and the more uniform penetration of the carbide based material, Fig. 13. In the latter case, the removal of carbide particles possibly assisted by the corrosion process at the particle/binder interface is the

predominant wastage mechanism . However, there is no evidence of through thickness loss of the coating to the substrate

(a) (b)

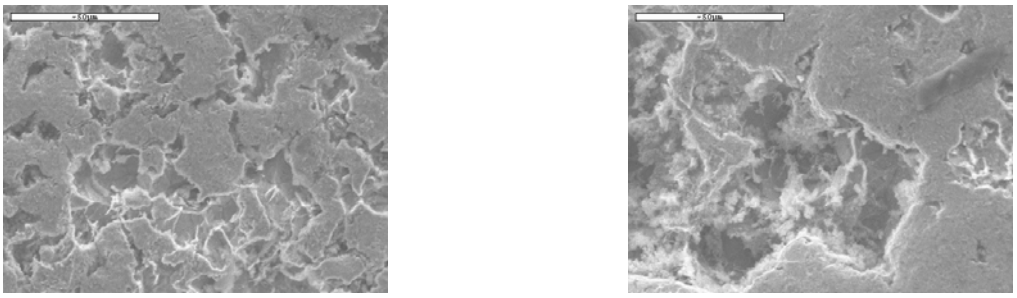

Fig. 12: SEM images of the eroded mild steel test specimen
(a) At 4% slurry concentration, 4 ms^{-1} impact velocity, E= -35mV
(b) At 8% slurry concentration, 4 ms^{-1} impact velocity, E= -35mV

(a) (b)

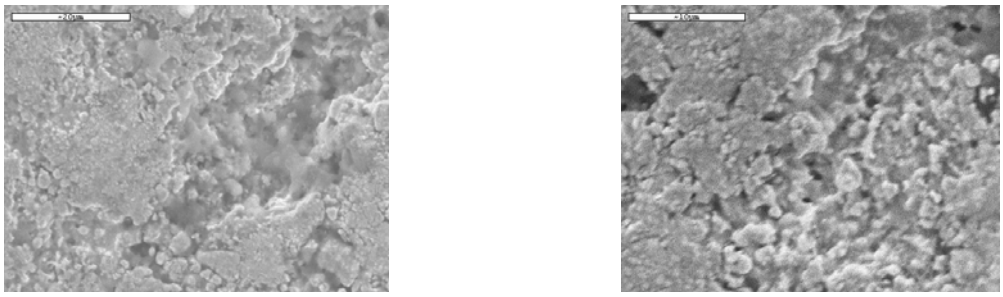

Fig. 13: SEM images of the eroded morphologies of the WC/Co-Cr coating
(a) At 4% slurry concentration, 4 ms^{-1} impact velocity, E= 500 mV
(b) At 8% slurry concentration, 4 ms^{-1} impact velocity, E= 500 mV

4.2 Interactions between erosion and corrosion

Previous work in erosion-corrosion has attempted to assign a basis for a systematic rationale on identifying regimes of erosion-corrosion behaviour. A first step is to subdivide the process into two components reflecting the tribological and corrosion

components on their own and two terms which represent the different interactions [5-8, 11]. From equation 2 above, it has been shown that the erosion-corrosion interaction can be expressed further as:

$$K_{ec}=K_{co}+K_{eo}+\Delta K_e+\Delta K_c \quad (3)$$

The erosion and corrosion contributions can be written as follows

$$K_e=K_{eo}+\Delta K_e \quad (4)$$

$$K_c=K_{co}+\Delta K_c \quad (5)$$

where, K_{ec}=erosion–corrosion rate, K_{eo}=erosion rate in the absence of corrosion, K_{co}=corrosion in the absence of erosion, ΔK_c=effect of erosion on corrosion (additive effect), ΔK_e=effect of corrosion on erosion (synergistic effect).

4.2.1 Erosion-corrosion mechanism maps

It is now a well established convention in aqueous erosion-corrosion research to describe regimes of erosion-corrosion on erosion-corrosion map [8, 13-14]. Erosion-corrosion maps can present the interaction between the erosion and corrosion process as functions of the main process parameters. The regimes on the maps are defined in terms of the following boundary conditions given below [8, 13-14]:

$K_e/ K_c \leq 0.1$ Corrosion (6)

$0.1< K_e/ K_c \leq 1$ Corrosion -Erosion (7)

$1< K_e/ K_c \leq 10$ Erosion-Corrosion (6)

$K_e/ K_c > 10$ Erosion (8)

The regimes can be subdivided further depending on the corrosion process taking place on the surface, with the corrosion term being replaced by dissolution, passivation transpassivation or pitting (identified by the polarization behaviour Figs. 10-11)

The various K_e/ K_c values for coated and uncoated material are calculated at each potential using data on Figures 6-9, indicating the individual contributions of both erosion and corrosion to the total erosion wastage. Erosion–corrosion mechanisms maps, Fig. 14, can be constructed using the above criteria, where the boundaries are defined a result of applied potential and slurry concentration at low and high impact velocities, i.e. 2 and 4 ms^{-1} respectively. The boundaries between the regimes are extrapolated by identifying the combinations of potentials and particle concentrations where the values of K_e/K_c change as identified above.

The erosion–corrosion maps, Fig. 14, are constructed for the coated and uncoated materials in sea water conditions showing the mechanistic interactions described above, based on the results, Figures 6-9, and the regime descriptions as described above.

These maps, Fig. 14(a-d), show the transition between erosion-corrosion mechanisms as a function of particle concentration and applied potential at two impact velocities.

Clearly the map, Fig.14a, indicates that at low concentrations (less than 6%) dissolution-erosion dominates at all potentials. However above this concentration, the mechanism shifts to erosion-dissolution where the erosion mechanism involves removal

of carbides (WC) by the larger number of particles in the slurry stream, as shown schematically, Fig.15.

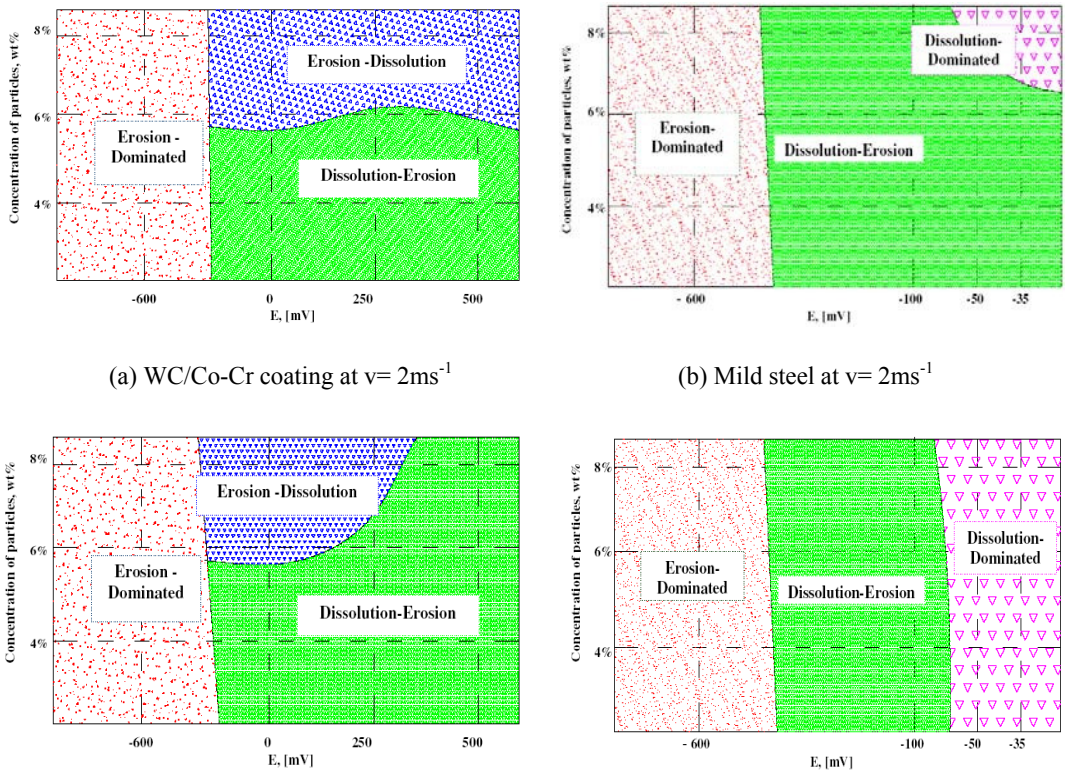

(a) WC/Co-Cr coating at v= 2ms^{-1} (b) Mild steel at v= 2ms^{-1}

(c) WC/Co-Cr coating at v= 4ms^{-1} (d) Mild steel at v= 4ms^{-1}

Fig. 14: Erosion–corrosion mechanism maps for the WC/Co-Cr coating and mild steel coating in sea water conditions showing the variation of the erosion–corrosion mechanisms as a function of slurry concentration and applied potential

In contrast to the behaviour observed for the coating, Fig. 14(a), the map for the mild steel, Fig. 14(b), indicates that the dissolution-erosion regime extends over a wide area where the anodic reaction takes place, with the exception to the behaviour observed at high particle concentrations. This dissolution regime shifts to lower particle concentrations at higher velocities, Fig. 14(d), indicating that increases in this parameter results in an increase in corrosion rate for this material. Not surprisingly, erosion

mechanisms predominate over all the concentrations and velocities tested, where the surface is exposed to cathodic potentials.

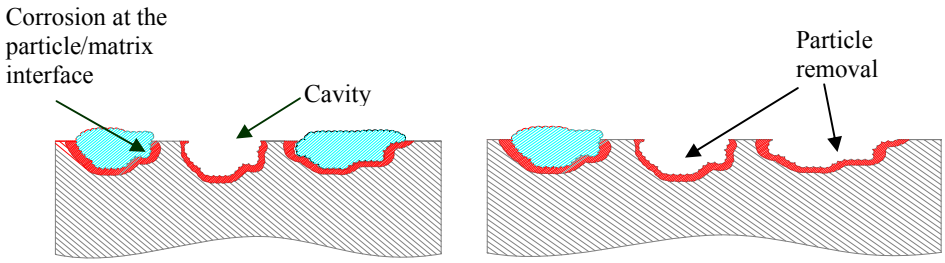

Fig. 15: Schematic diagram showing sequential stages of erosion-corrosion of the WC/Co-Cr coating.

The maps for the coating, Figs. 14(a,c) indicate that the dissolution-erosion regime extends to higher particle concentrations at the higher velocities, indicating an increase in corrosion contribution with increasing velocity. However, it is interesting that this increase is observed only at higher applied potentials and may, as discussed above, may be attributable to the higher mass transport of oxygen to the surface at such velocities. (As stated above, there may be subtle changes in the erosion-corrosion behaviour as identified on the weight change data, Fig. 6, due to the fact that this is a composite system. At this stage these subtleties have not been introduced into the erosion-corrosion mechanism map.)

4.2.2 Erosion-corrosion wastage maps

The mapping concept can also be used to chart transitions in wastage rates using simple limits of K_{ec} i.e. ranging from “low" to "medium" and "high". The limits for the wastage

boundaries will of course depend on the requirements of the materials and process specifically under investigation. In this case, the regime limits are defined [15] as the limits between the low-wastage regime corresponded to less or equal to 6 mg h^{-1} cm^{-2}, the medium-wastage regime between 6 to 50 mg h^{-1} cm^{-2} and the high wastage regime for the values greater than 50 mg h^{-1} cm^{-2}.

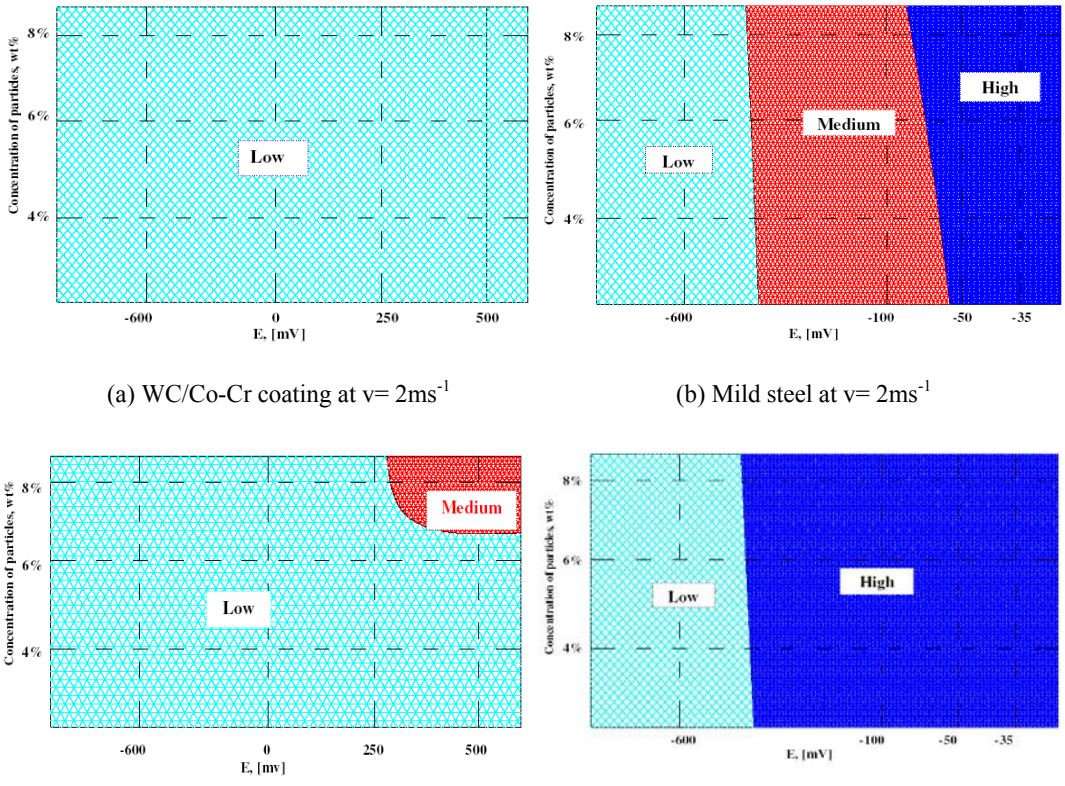

(a) WC/Co-Cr coating at v= 2ms^{-1}

(b) Mild steel at v= 2ms^{-1}

(c) WC/Co-Cr coating at v= 4ms^{-1}

(d) Mild steel at v= 4ms^{-1}

Fig. 16: Erosion–corrosion wastage maps for the coated and uncoated materials in sea water conditions based on the results showing the variation of the wastage regimes as a function of slurry concentration and applied potential

The maps for the coating and the substrate are shown in Figs. 16(a-d). These show that for the coating, the low wastage regime extends over the entire area of the map, Fig.

16(a), at low velocities (2 ms^{-1}). However at higher velocities, Fig.16(c), there is a transition to medium wastage at higher potentials as is expected with higher impact energy into the system. For the mild steel by contrast, Figs.16(b,d), the low wastage regime is only applicable to cathodic conditions as identified by the experimental data, Fig. 7 and 9. There is a transition to medium and high wastage as a function of increasing applied potential. Not surprisingly, at higher velocities, Fig. 16(d), the high wastage regime is enlarged with this regime extending to lower potentials. Thus in a very simple way, these maps indicate the significant differences between the wastage levels experience by the coating and steel in the slurry environment over the window of conditions tested in the study.

4.2.3 Erosion-corrosion additive-synergism maps

The significant advantage of sub-dividing regimes of erosion-corrosion behaviour is that it enables many different kinds of mechanistic interactions to be identified by mathematical manipulation of the terms in equation 2. Hence, a variety of diagrams can be generated based on these distinctions. An important aspect in any erosion-corrosion interaction is the extent to which corrosion affects the erosion behaviour versus how erosion affects the corrosion behaviour. In such cases, a methodology must be generated to identify which of these processes will predominate. A method of addressing this issue is to assign ratios to the so-called "additive" and "synergistic" terms as identified in equation 1. The following regime distinctions can be generated [15]:

$\Delta K_e/\Delta K_c \leq 0.1$ Additive (8)

$0.1<\Delta K_e/\Delta K_c \leq 1$ Additive-Synergistic (9)

$\Delta K_e/\Delta K_c > 1$ Synergistic (10)

"Negative synergism," is necessary to define and can be termed as "antagonistic" behaviour [8, 15]. Tables 2-3 indicate the values of $\Delta K_e/\Delta K_c$ ratio for the coated and uncoated substrate, showing the change in the ratio as a function of slurry concentration and applied potential at 2 and 4 ms^{-1} impact velocities.

The maps for the synergistic-additive contributions, Fig. 17(a-d), show that at low velocities, the relative contribution of synergistic versus additive erosion-corrosion behaviour is more pronounced for the coating by comparison to the substrate at the higher particle concentrations. Hence, “synergistic” effects are more dominant for the coating than for the substrate. This greater predominance of synergistic behaviour for the coating is, as discussed earlier, due to the action of the corrosion process at the interface between the carbide particles and the matrix and thus making the coating more vulnerable to wear, Fig. 15. Such observations for the coating are supported by the surface features as identified on the micrographs, Fig. 13.

The change in pattern for the coating at higher velocities, Fig. 17 (c), may at be due to the formation of an unstable film- possibly a salt film on the surface. It may also be due to incorporation of corrosion products (oxides), shown in the EDX analysis Fig.18, or sand particles in the matrix where carbide pull-out from the erosion process has

occurred. As discussed above, the erosion-corrosion of the composite material is possibly an amalgam of a wide range of possible interactions on the surface occurring during any one time interval. The assessment of which of these predominate over a range of experimental variables is the most important challenge for researchers in future work.

The synergistic effect observed at higher velocities for the mild steel, Fig. 17(d), may be due to the effects of pitting in the chloride solution making it more susceptible to erosion by the sand particles. Further work will be to investigate the basis of such regimes identified on these maps for both coating and substrate in order to identify the subtle mechanistic changes in the erosion-corrosion process as discussed above.

Table 2: $\Delta K_e/\Delta K_c$ values for the WC/Co-Cr coating and mild steel as a function of applied potential and slurry concentration at 2 ms^{-1}

(a) WC/Co-Cr at 4% slurry concentration

Potential	ΔK_c	ΔK_e	$\Delta K_e/\Delta K_c$
-600	0	0	
0	0.19	-0.26	-1.38
250	0.32	-0.05	-0.16
500	0.36	-0.1	-0.28

(b) WC/Co-Cr at 6% slurry concentration

Potential	ΔK_c	ΔK_e	$\Delta K_e/\Delta K_c$
-600	0	0	
0	0.05	-0.08	-1.69
250	1.004	-0.31	-0.31
500	0.14	0.27	1.93

(c) WC/Co-Cr at 8% slurry concentration

Potential	ΔK_c	ΔK_e	$\Delta K_e/\Delta K_c$
-600	0	0	
0	0.48	1.54	3.21
250	0.51	1.73	3.37
500	0.57	1.65	2.88

(d) Mild steel at 4% slurry concentration

Potential	ΔK_c	ΔK_e	$\Delta K_e/\Delta K_c$
-600	0	0	0
-100	10.69	4.45	0.42
-50	28.86	6.22	0.22
-35	28.18	5.28	0.19

(e) Mild steel at 6% slurry concentration

Potential	ΔK_c	ΔK_e	$\Delta K_e/\Delta K_c$
-600	0	0	
-100	7.44	2.68	0.36
-50	38.52	5.88	0.15
-35	43.56	8.69	0.20

(f) Mild steel at 8% slurry concentration

Potential	ΔK_c	ΔK_e	$\Delta K_e/\Delta K_c$
-600	0	0	
-100	37.65	3.52	0.09
-50	44.01	4.20	0.096
-35	54.27	4.93	0.09

Table 3: $\Delta K_e/\Delta K_c$ values for the WC/Co-Cr coating and mild steel as a function of applied potential and slurry concentration at 4 ms^{-1}

(a) WC/Co-Cr at 4% slurry concentration

Potential	ΔK_c	ΔK_e	$\Delta K_e/\Delta K_c$
-600	0	0	
0	0.79	-0.50	-0.63
250	0.21	-0.03	-0.12
500	0.64	-0.32	-0.50

(b) WC/Co-Cr at 6% slurry concentration

Potential	ΔK_c	ΔK_e	$\Delta K_e/\Delta K_c$
-600	0	0	
0	0.67	0.90	1.35
250	1.34	-0.65	-0.49
500	1.21	1.15	0.95

(c) WC/Co-Cr at 8% slurry concentration

Potential	ΔK_c	ΔK_e	$\Delta K_e/\Delta K_c$
-600	0	0	
0	0.79	1.28	1.63
250	1.58	0.69	0.44
500	5.40	0.02	0.004

(d) Mild steel at 4% slurry concentration

Potential	ΔK_c	ΔK_e	$\Delta K_e/\Delta K_c$
-600	0	0	
-100	32.85	5.23	0.16
-50	85.28	7.87	0.09
-35	163.17	5.36	0.03

(e) Mild steel at 6% slurry concentration

Potential	ΔK_c	ΔK_e	$\Delta K_e/\Delta K_c$
-600	0	0	
-100	56.22	7.33	0.13
-50	62.03	3.61	0.06
-35	150.93	12.85	0.09

(f) Mild steel at 8% slurry concentration

Potential	ΔK_c	ΔK_e	$\Delta K_e/\Delta K_c$
-600	0	0	
-100	78.78	6.17	0.08
-50	126.55	2.26	0.02
-35	202.72	3.51	0.02

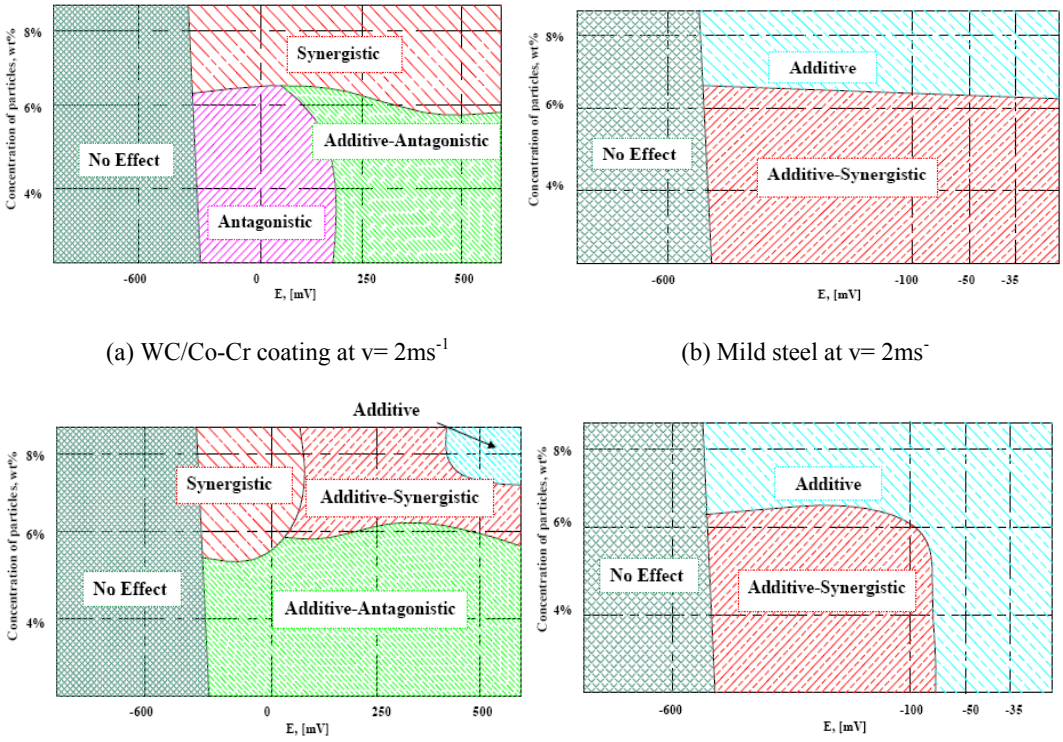

(a) WC/Co-Cr coating at v= 2ms^{-1} (b) Mild steel at v= 2ms^{-}

(c) WC/Co-Cr coating at v= 4ms^{-1} (d) Mild steel at v= 4ms^{-1}

Fig. 17: Erosion–corrosion additive-synergism maps for coated and uncoated materials as a function of slurry concentration and applied potential

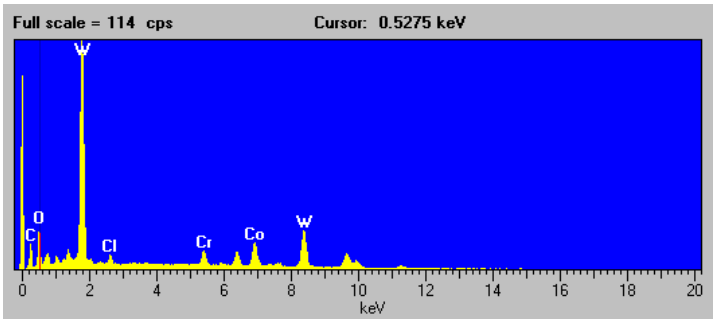

Fig. 18: EDX analysis of the coating following exposure to the erosion-corrosion test, showing evidence for formation of oxide film on the surface

4.2.4 Material performance maps

Finally, materials performance maps, Fig.19, can be developed as a function of applied potential and slurry concentration at 2 and 4 ms^{-1} by superimposing the low wastage regimes of Fig. 16 on a single space. The maps indicate the range of materials favoured under the conditions tested.

At low velocities (2 ms^{-1}), the map Fig. 19(a) indicates in cathodic conditions both the coating and the mild steel are favoured under the criteria outlined in the construction of the map. However, at higher potentials there is a change in performance with the coating favoured in preference to the steel which is due to the significantly lower wastage rates experience by the coatings as identified in Figs. 6, 8. This is also observed at higher velocities, Fig. 19(b).

Clearly such maps provide useful information on erosion-corrosion mechanisms, extent of synergy between the tribological and corrosion components and selection of materials and surface treatments. Future work in this area will be to identify using advanced microscopic techniques mechanistic changes in the erosion-corrosion process as functions of the variables addressed in this study in addition to developing mathematical models of the process by which these coatings are removed from the surface.

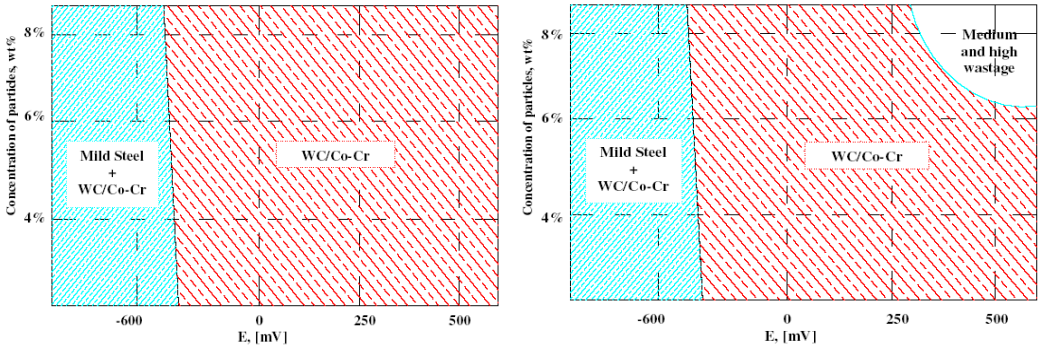

(a) (b)

Fig. 19: Material performance maps at impact velocities of (a) 2 ms^{-1} (b) 4 ms^{-1}

5. Conclusions

- The effects of slurry concentration and electrochemical potential on the erosion-corrosion behaviour of a WC/Co-Cr coating and a mild steel substrate have been assessed in sea water containing sand particles at various impact velocities.
- Mechanisms of erosion-corrosion have been identified for both the coating and the steel. Significant differences have been observed and these have been attributed to the interaction between erosion and corrosion of a monolithic material compared to a composite based coating. Various erosion-corrosion maps have been constructed based on the results, showing these interactions.
- Material performance maps have been developed based on the results showing that applied potential, slurry concentration and impact velocity can have a significant effect on the material optimization for the exposure conditions with marked changes in the performance envelope for both the coating and the steel when these parameters are varied.

6. References

1. C. Chuanxian, H. Bingtain and L. Huiling, "Plasma wear resistance of ceramic and cermet coating materials", Thin Solid Films 118 (1984) 485.
2. A. Karimi, C. Verdon and G. Barbezat, "Microstructure and hydroabrasive wear behaviour of high velocity oxy-fuel thermally sprayed WC–Co–(Cr) coatings", Surface and Coatings Technology, 57 (1993) 81.
3. M. Bjardal, E. Bardal, T. Rogne, T. G. Eggen, "Erosion and corrosion properties of WC coatings and duplex stainless steel in sand-containing synthetic sea water", Wear 186-187 (1995) 508.
4. J. Berget, E. Bardal, T. Rogne, "Effects of powder composition on erosion, corrosion, and erosion-corrosion properties of HVOF sprayed WC based coatings", Proc. Int. Thermal Spray Conf. 1 (1998) 305.
5. M. M. Stack and D. Pena, "Solid particle erosion of Ni-Cr/WC metal matrix composites at elevated temperatures: construction of erosion mechanism and process control maps**",** Wear 203-204 (1997) 489.
6. M.M. Stack and T.M. Abd El Badia, " On the construction of erosion-corrosion maps for WC/Co-Cr based coatings in aqueous conditions", Wear 261 (2006) 1181.
7. M.M. Stack, Y. Purandare and P. Hovsepian, "Impact angle effects on the erosion-corrosion of superlattice CrN/NbN PVD coatings", Surface and Coatings Technology 188-189 (2004) 556.
8. M.M. Stack and N. Pungwiwat, "Erosion–corrosion mapping of Fe in aqueous slurries: some views on a new rationale for defining the erosion–corrosion interaction", Wear 256 (2004) 565.

9. J. B. Zu, I. M. Hutchings, G. T. Burstein, "Design of slurry test rig", Wear 140 (1990) 331.
10. J. C. Myland and K. B. Oldham, "Uncompensated Resistance: The Effect of Cell Geometry" Analytical Chemistry 72 (2000) 3972.
11. M.M. Stack and B.D. Jana, "Modelling particulate erosion-corrosion in aqueous slurries: some views on the construction of erosion-corrosion maps for a range of pure metals", Wear, 256 (2004) 986.
12. M. M. Stack, J. S. James and Q. Lu, "Erosion–corrosion of chromium steel in a rotating cylinder electrode system: some comments on particle size effects", Wear 256 (2004) 557.
13. M. M. Stack, N. Corlett and S. Turgoose, "Some thoughts on modelling the effects of oxygen and particle concentration on the erosion–corrosion of steels in aqueous slurries" Wear 255 (2003) 225.
14. M.M. Stack and B.D. Jana, "Modelling particulate erosion–corrosion regime transitions for Al/Al_2O_3 and Cu/Al_2O_3 MMCs in aqueous conditions", Tribology International 38 (2006) 995.
15. M.M. Stack and T.M. Abd El Badia, "Mapping erosion–corrosion of WC/Co–Cr based composite coatings: Particle velocity and applied potential effects", Surface and Coatings Technology 201 (2006) 1335.

7. Captions for figures

Fig.1: EDX analysis of the coating [6]

Fig. 2: Optical microscopy of cross section of the coating morphology [6]

Fig. 3: Silica sand used in the erosion–corrosion tests

Fig. 4: Slurry impingement erosion test rig based on the design of Zu et al [9].

Fig. 5: The electrochemical configuration of the three electrode cell used in erosion-corrosion tests

Fig. 6: Mass loss rates for the WC/Co-Cr coating as a function of applied potential at 2 ms^{-1} impact velocity

Fig. 7: Mass loss rates for mild steel as a function of applied potential at 2 ms^{-1} impact velocity

Fig. 8: Mass loss rates for the WC/Co-Cr coating as a function of applied potential at 4 ms^{-1} impact velocity

Fig. 9: Mass loss rates for mild steel as a function of applied potential at 4 ms^{-1} impact velocity

Fig. 10: Polarization curve for
the WC/Co-Cr coating

Fig. 11: Polarization curve for
mild steel

Fig. 12: SEM images of the eroded mild steel test specimen

(a) At 4% slurry concentration, 4 ms^{-1} impact velocity, E= -35mV

(b) At 8% slurry concentration, 4 ms^{-1} impact velocity, E= -35mV

Fig. 13: SEM images of the eroded morphologies of
the WC/Co-Cr coating

(a) At 4% slurry concentration, 4 ms^{-1} impact velocity, E= 500 mV

(b) At 8% slurry concentration, 4 ms^{-1} impact velocity, E= 500 mV

Fig. 14: Erosion–corrosion mechanism maps for the WC/Co-Cr coating and mild steel coating in sea water conditions showing the variation of the erosion–corrosion mechanisms as a function of slurry concentration and applied potential

Fig. 15: Schematic diagram showing sequential stages of erosion-corrosion of the WC/Co-Cr coating

Fig. 16: Erosion–corrosion wastage maps for coated and uncoated materials in sea water conditions based on the results showing the variation of the wastage regimes as a function of slurry concentration and applied potential

Fig. 17: Erosion–corrosion additive-synergism maps for coated and uncoated materials as a function of slurry concentration and applied potential

Fig. 18: EDX analysis of the coating following exposure to the erosion-corrosion test, showing evidence for formation of oxide film on the surface.

Fig. 19. Erosion-corrosion materials performance map based on the results.

8. Captions for tables

Table 1: Composition of the coating tested

Table 2: $\Delta K_e/\Delta K_c$ values for the WC/Co-Cr coating and mild steel as a function of applied potential and slurry concentration at 2 ms^{-1}

Table 3: $\Delta K_e/\Delta K_c$ values for the WC/Co-Cr coating and mild steel as a function of applied potential and slurry concentration at 4 ms^{-1}